

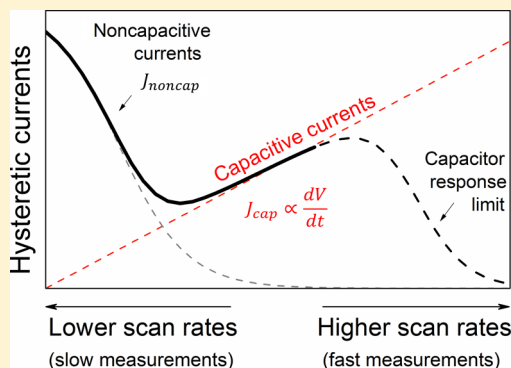
Noncapacitive Hysteresis in Perovskite Solar Cells at Room Temperature

Osbel Almora, Clara Aranda, Isaac Zarazua, Antonio Guerrero, and Germà Garcia-Belmonte*

Institute of Advanced Materials (INAM), Universitat Jaume I, 12006 Castelló, Spain

Supporting Information

ABSTRACT: The current density–voltage (J – V) curves of perovskite solar cells have been found to present a hysteresis-like distortion when the measurement is done by sweeping the applied voltage at different scan conditions. Hysteresis has raised many concerns about the feasibility and long-term stability of this kind of photovoltaic technology. However, there is a lack of distinction among different hysteretic phenomena which is necessary to unravel its underlying physical and chemical mechanisms. Here we distinguish between capacitive and noncapacitive currents giving rise to specific hysteretic responses in the J – V curves of PSCs. It is reported that capacitive current causing hysteresis dominates in regular structures with TiO_2 as bottom electron selective layer. This is mainly caused by the charge, both ionic and electronic, accumulation ability of the TiO_2 /perovskite interface but has no influence on the steady-state operation. Noncapacitive hysteresis is observable at slow enough scan rates in all kind of architectures. Inverted structures, including organic compounds as bottom hole selective layers and fullerene materials as top contact, exhibit larger noncapacitive distortions because of the inherent reactivity of contact materials and absorber perovskites.



The current density–voltage (J – V) curves of perovskite solar cells (PSCs) have been found to present a hysteresis-like distortion when the measurement is done by reversing the sweeping sense of the applied voltage.¹ Hysteretic effect is characterized by the presence of additional currents J_{hyst} that modify the operating response of the cells. Silicon solar cells have been reported to show hysteresis at very fast J – V measurements² caused by capacitive effects, and also polycrystalline CdS/CdTe thin-film solar cells exhibited transient distortions depending on the sweep direction because of ion migration.³ Hysteresis effects have not been reported for other photovoltaic technologies such as dye or organic solar cells. Presumably the fact that halide perovskites exhibit ionic conduction⁴ lies behind the prominent hysteretic response of cells comprising these compounds. Observation of hysteresis has raised many concerns about the feasibility and long-term stability of this kind of photovoltaic technology. A strong dependence on bias scan rate $s = \Delta V/\Delta t$ has been widely identified; that is, the difference in current between the forward bias scan (FS) and the backward bias scan (BS) changes depending on the applied voltage sweep velocity (or delay time between measurement points). There have been many reports showing the hysteresis phenomenology, as well as explanation attempts focusing on its origin mechanisms. For instance, while many authors have observed a qualitative increase of the hysteretic effect as the scan rate is augmented,^{5–12} others have found the opposite.^{1,13–16} However, each one of these studies

analyzed a restricted range of scan rates. A classification able to cover different hysteretic phenomenologies which can be used as a basis to progress into their underlying physical and chemical processes is needed. Recent reports have identified the occurrence of capacitive currents distorting the response of PSCs both in the dark and under illumination.^{7,12} Capacitive currents originate from the charging–discharging dynamics of capacitors of dielectric nature linked with the ionic polarization of outer electrodes¹⁷ and also light-induced electronic accumulation surface layers¹⁸ confined within the Debye length in the vicinity of the contacts. In both cases capacitive currents exhibit larger contributions as the scan rate is increased

$$J_{\text{cap}} = Cs \quad (1)$$

where C is the device capacitance per unit area. The proportionality between scan rate and hysteretic current is actually observed for perovskite solar cells comprising TiO_2 as electron collecting material.¹⁹ The reported values for the capacitance are too large to stem from a geometric or chemical origin.²⁰ A distinctive feature of capacitive hysteresis appears approaching steady-state conditions: it should vanish as the scan rate is reduced. Here we show how at extremely low scan rates the hysteretic response is still present, being hardly

Received: May 4, 2016

Accepted: May 31, 2016

connected to the capacitive contribution previously outlined. It is also observed that PSCs containing organic or fullerene layers do exhibit prominent noncapacitive hysteretic contributions exceeding those observed for regular architectures made up of TiO₂ bottom layers, either mesoscopic or planar. Noncapacitive hysteresis is connected here to the reactivity at the contact interlayers.

In this work we explore the current density and capacitance responses to applied voltage of several PSC structures in a wide range of scan rates with the purpose of discerning between capacitive and noncapacitive hysteretic currents. The nomenclature and structure (see inset of Figures 1b,c and S2a) of the analyzed devices are summarized in Table 1. Also listed are the respective photovoltaic parameters extracted from room-temperature J - V curves of Figure S1, where it is observed how hysteresis is evidently present in regular samples (RegularFlat and RegularMeso), that we will label as “hysteretic devices”. On the other hand, the inverted structures comprising organic and fullerene-based interlayers result in practically “hysteresis-free devices” under illumination, as usually reported.

In order to distinguish among the possible contributions to PSCs hysteresis, it is useful to analyze dark J - V curves under a wide range of scan rates. These measuring conditions avoid an extra parameter (light) to induce significant degradation^{21,22} (mainly during long-term measurements). Furthermore, the light soaking has been found to influence hysteretic currents,^{8,9,23} but it is not their primary cause because hysteresis behaves similarly in some cases in dark J - V curves.^{8,24} In general terms, hysteretic currents appear in addition to operating currents, $J = J_{\text{oper}} + J_{\text{hyst}}$. One of the contributions to J_{hyst} is J_{cap} , which dominates at intermediate scan rates. The dark J - V curve representation, with logarithm scaled current densities, straightforwardly illustrates the effect of capacitive currents, as shown in the simulation of Figure 1a (red solid lines) and in the experimental dark J - V response of RegularMeso device in Figure 1b (Figure S2a for RegularFlat). The overall effect of capacitive currents is a mere addition or subtraction equaling eq 1, depending of the scan rate sign, that yields a squarelike current response around zero bias.^{7,25} As the applied bias sweep speed is slowed down (or delay time between measurement points increases), J_{cap} gradually reduces until the hysteresis effectively vanishes as FS and BS dark J - V curves collapse into the steady-state response. Here, current must be negligible at zero applied voltage (see low-voltage region in Figure 1a, black solid line) because the capacitive contribution disappears. Before a steady-state condition is reached, J_{cap} can be evaluated as the average between the absolute current densities in FS and BS at zero volts (Figure 1a between red arrows). This capacitive hysteresis feature have been also unambiguously identified for regular FTO/TiO₂/MAPbI_{3-x}Cl_x/spiro-OMeTAD/Au (planar and mesoporous structures).⁷ Here, two other regular structures (RegularFlat and RegularMeso, in Table 1) are also tested. It can be seen (J - V curve under illumination in Figure S1, as well as from dark J - V curves in Figures 1b and S2a) that RegularFlat and RegularMeso samples show pronounced capacitive hysteresis. Specifically, in the dark J - V curves at different scan rates of these devices a characteristic linear trend as $J_{\text{cap}} = C \cdot s$ is observed, which is displayed in Figure S2b.

It has been widely reported that PSC capacitance presents an increase of several orders of magnitude at low frequencies.^{7,10,12,20,26} This giant low-frequency capacitance has been directly related to the hysteretic effect on J - V curves.^{6,7,10,12}

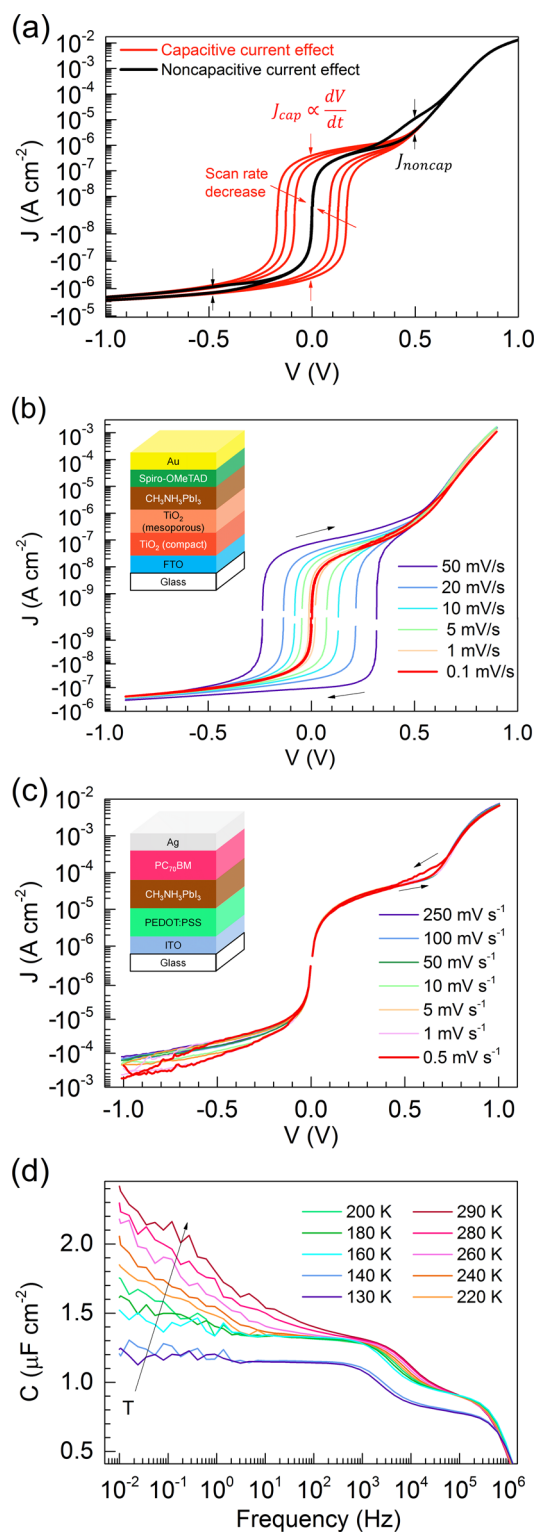


Figure 1. Dark J - V curves at room temperature in logarithm scaled current representation: (a) simulation illustrating different hysteretic effects as a function of the scan rate during the bias sweep in both senses; experimental data from (b) RegularMeso and (c) Inverted PSCs at different scan rates with corresponding structures sketched in the insets; and (d) dark capacitance spectra of Inverted sample for a wide frequency range at different temperatures, as indicated.

Here, the capacitance spectra of our “hysteretic samples”, as illustrated in Figure S2c, also exhibit such an effect. Hence,

Table 1. Nomenclature, Structure, and Parameters (See Figure S1 J – V Curves)^a

label	structure	J_{sc} (mA cm ⁻²)	V_{oc} (mV)	FF (%)	PCE (%)
RegularFlat	FTO/cTiO ₂ /MAPbI ₃ /spiro-OMeTAD/Au	18.3	1037	67.4	12.8
RegularMeso	FTO/cTiO ₂ /mTiO ₂ /MAPbI ₃ /spiro-OMeTAD/Au	20.1	943	67.5	12.8
Inverted	ITO/PEDOT:PSS/MAPbI ₃ /PC ₇₀ BM/Ag	16.8	810	53.6	7.3

^aFor simplicity, only the backward scan (BS) was considered in those devices with remarkable hysteresis. Here, J_{sc} stands for the short circuit current; V_{oc} is the open circuit current, FF the fill factor, and PCE the light-to-electric current power conversion efficiency; MA in MAPbI₃ is methylammonium (CH₃NH₃), and cTiO₂ or mTiO₂ stand for compact or mesoporous TiO₂ layers, respectively.

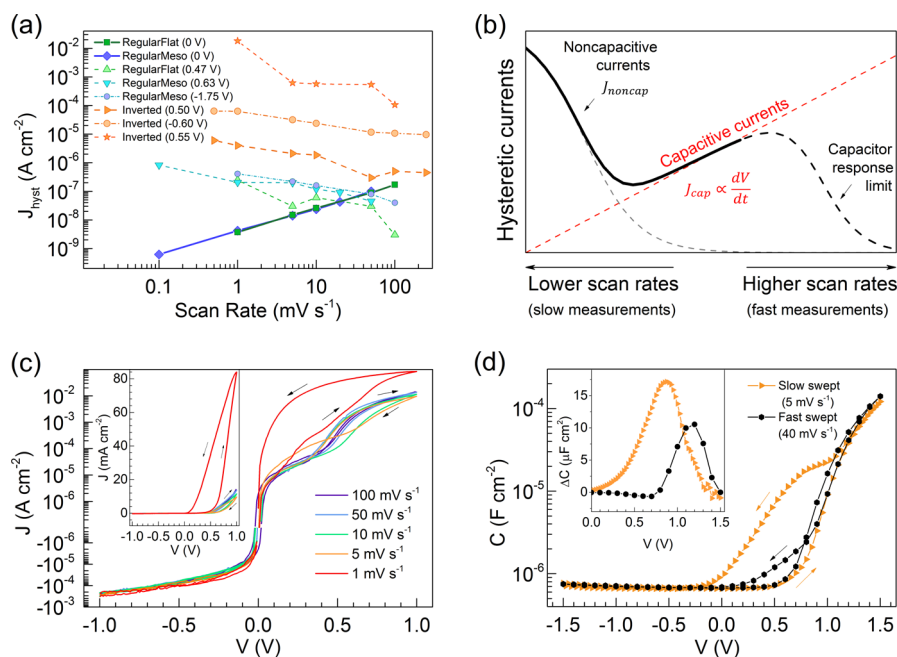


Figure 2. (a) Experimental dark hysteretic currents as a function of scan rate, calculated as the average current between scan senses at the indicated applied voltages for J – V curves of Figures 1b,c and S2a. The data points with star symbols represent maximum hysteresis of the inverted sample in Figure 2c. When J_{hyst} is evaluated in zero volts, the hysteretic current is J_{cap} (solid lines); elsewhere, it is J_{noncap} (dashed lines). (b) Sketch of general behavior of hysteretic currents with scan rate showing three regions dominated by noncapacitive currents, capacitive currents, and the response limitation of the sample capacitor. (c) Dark J – V curves in logarithmic scaled currents representation for an Inverted sample at room temperature and different scan rates. Inset in panel c shows the same curves but in linear scaled current representation. (d) Dark capacitance–voltage curves of Inverted sample in panel c at two different scan rates, as indicated. Inset in panel d is the capacitance difference, ΔC , between scan senses for both scan rates. The AC perturbation was 10 mV at 10 kHz.

large low-frequency capacitances promote hysteresis effect, in the form of capacitive currents. Supporting this statement it is observed that PSCs with small low-frequency excess capacitance exhibit “hysteresis-free” (or considerably reduced) responses at room temperature.²⁷ Inverted structured devices, characterized by the use of organic selective contacts sandwiching the absorber perovskite, are the most commonly reported hysteresis-free PSCs (summarized in Table S1). Consequently, we performed dark J – V curve measurements in a wide scan rate range (0.5–250 mV·s⁻¹) for inverted configured devices, as illustrated in Figure 1c. Indeed, at low voltages there is no trace of capacitive current at room temperature; that is, regardless of the scan rate or sense, the current is always negligible at zero volts. The capacitance spectra at different temperatures for inverted solar cells (Figure 1d) exhibit the earlier described⁷ progressive increase in capacitance with temperature, including a gap around the MAPbI₃ crystal phase transition from β -tetragonal to γ -orthorhombic at 150 K.²⁸ In addition, the capacitance spectrum of samples without perovskite layer (ITO/PEDOT:PSS/PC₇₀BM/Ag) was explored, which exhibits a constant capacitance of 0.8 $\mu\text{F}\cdot\text{cm}^{-2}$ (Figure S3). This value lies below

that exhibited for complete inverted solar cells (1.3 $\mu\text{F}\cdot\text{cm}^{-2}$) at room temperature, ensuring that the capacitance response is certainly dominated by the perovskite layer. Interestingly, the excess capacitance at low frequency of inverted cells (Figure 1d) just doubles the capacitance at the plateau around 1 kHz, but no significant increase occurs as that observed for solar cells containing TiO₂ layers, in agreement with previous reports.²⁷ With these low capacitance values the capacitive hysteresis effect would be observable only at scan rates larger than 5 V·s⁻¹ because $J_{\text{cap}} = C \cdot s$. Capacitance spectra then agree with the absence of substantial capacitive currents causing hysteresis for inverted structures.

Capacitive hysteresis in the dark has been suggested to originate from the perovskite’s ability to transport ionic species which accumulate at the TiO₂ interface.⁷ The fact that PCBM/perovskite interface does not exhibit pronounced capacitive features indicates that ionic migration is a necessary but not sufficient condition for hysteresis to be induced. The interplay between ionic conduction and interface interaction is needed to enhance charge accumulation and consequently hysteretic behavior. The specific contact interactions between TiO₂ and halide perovskites have been studied by De Angelis and co-

workers.²⁹ This computational calculation indicates that a weak interaction occurs mainly through the binding of perovskite iodine atoms to under-coordinated Ti(IV) atoms of the TiO₂ surface. Ti–I bonds easily accommodate excess or defect ionic charge in a highly reversible way causing the capacitive currents. Under illumination, the low-frequency capacitance is largely increased²⁰ and hysteretic light J – V curves are prominent.¹² However, these light-induced effects are hardly interpreted relying exclusively on ionic mechanisms. At the present time we can only speculate about the necessary local interplay between ionic species and photogenerated carriers at the contact/perovskite interface able to enhance hysteretic responses.¹⁸

So far, we have highlighted how capacitive currents $J_{\text{cap}} = C \cdot s$ are behind a specific case of hysteretic behavior in PSCs, appreciated at low voltage in dark J – V curves, and their correlation with the low-frequency capacitance. The experimentally obtained J_{cap} values for the “hysteretic samples” are also plotted in Figure 2a. These values are directly measured from the J – V curves in Figure 1b at zero bias. As expected, capacitive current increases linearly as the scan rate is increased, but it does not influence the solar cell performance in a detrimental manner as it vanishes at steady state. However, when slow enough voltage sweeps are performed, instead of a hysteresis-free steady-state dark J – V curve, a new kind of hysteretic distortion arises mainly around 0.5 V at forward bias, but also in reverse bias. This behavior is sketched in the simulation of Figure 1a (black solid lines), and it can be also seen in the slowest dark J – V curves of the “hysteresis-free” Inverted sample in Figure 1c (also for regular “hysteretic devices” in Figures 1b and S2a). This is indeed a new feature different from the previously discussed capacitive hysteresis, which relates to reports on hysteresis increment with scan rate decrease (or longer delay time between measurement points).^{13,14,16}

It is convenient to quantify the absolute hysteretic currents from the difference between forward and backward current densities at selected voltages. Additional hysteretic current contributions for each sample at individual critical voltages (different from zero bias) at low scan rate are presented with dotted dashed line curves in Figure 2a. It is also included in data from a particularly hysteretic Inverted sample (in Figure 2c) and the RegularMeso sample in high reverse polarization regime (in Figure S4) given that the hysteresis at reverse bias has been also earlier reported in several device structures.^{30,31} When Figure 2a is examined, it is appreciated that hysteretic currents increase as the scan rate decreases and that for the inverted devices (that do not exhibit J_{cap}) this current component is in general larger than for the “hysteretic samples” of regular architecture.

We will henceforth denote as noncapacitive hysteretic currents (J_{noncap}) the slow scan rate distortion in J – V curves to differentiate it from the previously discussed J_{cap} . Accordingly, the total hysteretic current behavior can be schematically summarized in Figure 2b where three scan rate regions are defined: (i) at extremely low s , noncapacitive currents appear for all kind of architectures; (ii) at intermediate s , capacitive currents are present with $J_{\text{cap}} = C \cdot s$ in regular structures; and (iii) at high s , capacitive current is limited by the capacitor response time constant. The hysteresis disappears at larger scan rates because the response RC time constant is longer than the measuring time inhibiting as a consequence the capacitance charging. This is in agreement with previous observations of hysteresis reduction at high scan rates.^{8,13} When

the sample capacitance is large, at high enough scan rates a linear trend arises between J_{hyst} and s . This feature signals the occurrence of capacitive currents as observed in the dark as well as in J – V curves under illumination.^{7,12} Finally, at the lowest scan rates, only noncapacitive currents can rule the hysteresis as capacitive currents vanish. Noncapacitive hysteresis is a general signature observed both for regular and inverted structures. However, it is the dominant hysteretic mechanism for devices with inverted configuration. We note here that a different effect is produced by bias preconditioning under illumination⁸ that causes changes in photocurrent induced by ionic contact barrier modification.

The previous analysis allows us to write a general form for the dark current including terms accounting for both operating and hysteretic contributions

$$J = J_0 \left[\exp\left(\frac{qV}{nk_B T}\right) - 1 \right] + \frac{V}{R_{\text{sh}}} + J_{\text{cap}} + J_{\text{noncap}} \quad (2)$$

The two first terms model the operating currents. The first summand corresponds to the dark diode equation with J_0 accounting for the saturation current; q is the elementary charge, $k_B T$ the thermal energy, and n the ideality factor. The second term accounts for the leakage currents with R_{sh} representing the specific shunt resistance. For the sake of clarity, we assume negligible series resistance, R_s , which slightly corrects the voltage within the cell. Hysteretic currents are divided into either capacitive J_{cap} , as already introduced in eq 1, or noncapacitive J_{noncap} . For the simulated curves of J_{noncap} in Figure 1a, we have selected an empirical equation, similar to that of the Nernst–Monod model³²

$$J_{\text{noncap}} = J_{\text{max}} \left[1 + \exp\left(-\frac{q(V - V_0)}{nk_B T}\right) \right]^{-1} \quad (3)$$

Equation 3 can be assimilated to a steplike behavior that attains J_{max} for positive potentials $V > V_0$. The characteristic voltage V_0 establishes the current onset and is related to a reaction potential. In our simulation, J_{noncap} is introduced only during the RS because long-term positive polarization activates ionic reaction as next explained. Similar contributions can be observed in Figure 1a for $V < 0$. It is clear that more general models, relying on Nernst and Butler–Volmer equations, can be also devised accounting for J_{noncap} . Equation 3 tries to capture the essential phenomenology in a simple manner.

Noncapacitive currents can be observed in the J – V curves of Figure 2c for particularly hysteretic inverted PSCs. A huge difference between FS and BS currents appears at positive bias that enlarges as the scan rate is reduced. This fact rules out the occurrence of capacitive currents in this type of solar cells as previously discussed. To corroborate that the observed low scan rate hysteretic response really has a noncapacitive origin, capacitance at a given frequency was measured at different scan rates. Figure 2d shows the capacitance as a function of voltage for inverted samples at two scan rates. As observed, the measured capacitance exhibits only minor variation on s at FS voltage sweep. The capacitance is constant at negative and low-voltage (related to the geometrical value), while the capacitance increases at forward voltage as a consequence of previously mentioned accumulation processes. However, the reverse voltage sweep produces an increment of almost 1 order of magnitude in the capacitance. Furthermore, the difference between forward and reverse sweeps is enhanced around 0.5 V

as the scan rate is slowed in good agreement with the difference in current of Figure 1c. The nature of this capacitance modification with the bias scan rate (or time of polarization) cannot be simply explained by recalling capacitive models as ionic electrode polarization or chemical capacitance. Moreover, depletion capacitance modifications giving rise to changes in Mott–Schottky plots do not seem proper explanations of the observation in Figure 2d. Therefore, other phenomena must be considered in order to explain the capacitance increase, like in the Figure 2d inset, that takes place at low scan rate.

The previous experimental results point to the occurrence of a complex scenario in which long-term degradation or aging mechanisms deteriorate the solar cell response, altering both J – V curves and direct capacitive measurements. A recent analysis¹³ also divided the hysteretic effect in three regions as a function of the scan rate but associated the low scan range hysteretic currents with ferroelectric effects. An interesting observation with still unclear origin is the severe illuminated J – V curve hysteresis³³ observed for inverted PSCs at low temperature and high scan rates. This behavior is in contrast with previous results in regular configurations (TiO₂/MAPbI₃/spiro-OMeTAD) for which hysteresis is diminished with temperature;^{34,35} however, photogeneration of charges changes with temperature in MAPbI₃ as recently claimed.³⁶ In any case, the prominent hysteretic behavior exhibited by inverted devices does not correspond to J_{cap} contributions because the capacitance slightly increases with temperature, as shown in Figures 1d and S5a. In contrast, the predominance of capacitive currents is well observed in the regular PSCs configuration, as presented for the RegularMeso sample dark J – V curves of Figure S5, where capacitance decrease by lowering temperature, as does J_{cap} . In addition, we recorded dark J – V curves at low temperatures (see Figure S5b), and a small increase of the hysteretic currents appeared at higher voltages, not comparable to those exhibited by inverted samples at the slowest scan rate.

Finally, we stress here that the occurrence of noncapacitive currents could be explained by the presence of chemical reactions, as recently suggested.^{19,37} Slow scan rates implies long-time solar cell polarization, which may induce ionic migration and consequently chemical interactions with the contacting layers. Noncapacitive current can be then assimilated to Faradaic currents commonly found in electrochemical experiments. Our parametrization of noncapacitive currents in eq 3 tries to capture this observation. When measuring in FS at slow scan rates, dark current slightly deviates from the undistorted J_{oper} . Positive polarization induces J_{noncap} that is later reduced during the RS for voltages $V < V_0$. The characteristic potential $V_0 \approx 0.5$ V would be connected to the reactivity of the perovskite/interlayer interface. Similar contributions can be encountered for negative potentials. For regular structures, the interaction between iodine anions and spiro-OMeTAD⁺ has been identified, producing an irreversible redox peak superimposed to the operation J – V curve.¹⁹ The interaction is observable only at slow scan rates as observed in Figures 1b and S2a,b. It progressively reduces the hole-transporting material's conductivity and deteriorates the solar cell performance. For inverted structures, the importance of buffer layers to avoid the chemical reactivity of the perovskite with the external contacts has been highlighted. Excess iodide anions at the cathode promote chemical interactions with both the fullerene interlayer³⁸ and the top metallic contact giving rise to corrosion and overall performance degradation.³⁷ All these chemical reactions yield observable distortions in the J – V and

C – V curves interpreted here as noncapacitive hysteretic currents.

In summary, our approach allows us to distinguish between capacitive and noncapacitive currents originating specific hysteretic responses in the J – V curves of PSCs. It is reported that capacitive hysteresis dominates in regular structures. This is mainly caused by the charge, both ionic and electronic, accumulation ability of the TiO₂/perovskite interface. Capacitive hysteresis does not influence the solar cell performance as it vanishes at steady state. Noncapacitive hysteresis is observable at slow enough scan rates in all kind of architectures. Inverted structures exhibit larger noncapacitive distortions because of the inherent reactivity of contact materials and absorber perovskites. Hence, chemical interactions at contacts become an issue of primary concern for the applicability of this solar technology.

EXPERIMENTAL SECTION

Characterization. Illuminated J – V curves were performed under 100 mW·cm^{−2} of AM1.5G light spectrum with a Sun 2000 system solar simulator from Abet Technologies. For the dark J – V curve, a PGSTAT-30 potentiostat from Autolab was used. Dark capacitance measurements at room and lower temperatures via impedance spectroscopy were made by using an Alpha-N analyzer with a Quatro Cryosystem temperature controller from Novocontrol Technologies.

RegularFlat and RegularMeso Samples Fabrication. The two studied regular configuration cells were prepared over FTO coated glasses (25 × 25 mm, Pilkington TEC15, ~15 Ω/sq resistance), which were partially etched with zinc powder and HCl (2 M) to avoid short circuits, obtaining 0.25 cm² of active electrode area. The substrates were cleaned with soap (Hellmanex) and rinsed with Milli-Q water and ethanol. Then, the sheets were sonicated for 15 min in a solution of acetone:isopropanol (1:1 v/v), rinsed with ethanol, and dried with compressed air. After that, the substrates were treated in a UV–O₃ chamber for 10 min. For the growth of the electron transport material (ETM) film, the TiO₂ blocking layer was deposited onto the substrates by spray pyrolysis at 450 °C, using a titanium diisopropoxidebis(acetylacetonate) (75% in isopropanol, Sigma-Aldrich) solution diluted in absolute ethanol (0.2 M), with oxygen as carrier gas. The spray was performed in 3 steps of 6 s, spraying a total of 5 mL (approx.), and waiting 30 s between steps. After the spraying process, the films were kept at 450 °C for 30 min. When needed, for cells with mesoporous scaffold (RegularMeso), the mesoporous TiO₂ layer was deposited by spin coating 100 μL at 2000 rpm during 10 s using a TiO₂ paste (Dyesol 30NRd, 30 nm average particle size) diluted in ethanol (1:5, weight ratio). After drying at 100 °C for 10 min, the TiO₂ mesoporous layer was heated at 500 °C for 30 min and later cooled to room temperature. Samples were transferred to a nitrogen filled glovebox equipped with a thermal evaporator. The perovskite precursor solution was prepared following the process reported by Ahn et al.³⁹ A 50 μL perovskite solution containing MAI (Dyesol), PbI₂ (TCI, 99.999%), and DMSO (1:1:1 mol %) in a DMF solution (50 wt %) is spin coated at 4000 rpm for 50 s with acceleration of 4000 rpm. Nonpolar diethyl ether was poured onto the spinning substrate after the initial 5–7 s to selectively wash the DMF. A transparent film generated after the spin coating and a heat treatment at 65 °C for 1 min was effective to remove the DMSO, and shiny and dark brown MAPbI₃ films were obtained by further annealing at 100 °C for 2 min. Then, the perovskite

films were covered with the hole-transporting material (HTM) by spin coating at 4000 rpm for 30 s under nitrogen conditions, using 50 μL of spiro-OMeTAD solution. The spiro-OMeTAD solution was prepared by dissolving in 1 mL of chlorobenzene 72.3 mg of (2,2',7,7'-tetrakis(*N,N'*-di-*p*-methoxyphenylamine)-9,9'-spirobifluorene), 28.8 μL of 4-*tert*-butylpyridine, and 17.5 μL of a stock solution of 520 mg/mL of lithium bis-(trifluoromethylsulfonyl)imide in acetonitrile. Finally, 60 nm of gold was thermally evaporated on top of the device to form the electrode contacts using a commercial Univex 250 chamber, from Oerlikon Leybold Vacuum. Before the beginning of the evaporation, the chamber was evacuated to a pressure of 2×10^{-6} mbar. The active electrode area of 0.25 cm^2 per pixel is defined by the FTO and the Au contacts.

Inverted Samples Fabrication. As the first step, the HTM was deposited on top of ITO-covered glass substrates (20×20 mm, Xin Yan Tech. XY10S; $\sim 10 \Omega/\text{sq}$ resistance). The substrates were previously cleaned with soap (Hellmanex) and rinsed with Milli-Q water. Then, the sheets were sonicated for 15 min in soapy Milli-Q water, rinsed with Milli-Q water, once more sonicated for 15 min but in ethanol, later rinsed with acetone and finally dried with compressed air. After that, the substrates were treated in a UV- O_3 chamber for 15 min. Subsequently, the poly(3,4-ethylenedioxythiophene) doped with poly(4-styrenesulfonate) (PEDOT:PSS, Baytron P AI 4083) was deposited by spin-coating at 6000 rpm for 60 s. The perovskite absorber layer was fabricated following the same process as that described previously for RegularFlat and RegularMeso. Successively, the ETM layer was prepared by spin coating a solution containing [6,6]-phenyl-C-71-butyric acid methyl ester (PC₇₀BM, Solenne, 99.5%) in chlorobenzene (50 mg/mL) at 1000 rpm during 30 s. Finally, the ITO/PEDOT:PSS/MAPbI₃/PC₇₀BM film was transferred to a vacuum chamber for coating the Ag (60 nm) electrode.

■ ASSOCIATED CONTENT

Supporting Information

The Supporting Information is available free of charge on the ACS Publications website at DOI: [10.1021/acseenergylett.6b00116](https://doi.org/10.1021/acseenergylett.6b00116).

Light *J*-*V* curves of analyzed structures, *C*-*V* and capacitance spectra of planar and mesoscopic cells, along with dark *J*-*V* curves as a function of temperature (PDF)

■ AUTHOR INFORMATION

Corresponding Author

*E-mail: garciag@uji.es. Tel.: +34 964 387538.

Notes

The authors declare no competing financial interest.

■ ACKNOWLEDGMENTS

We acknowledge financial support by Ministerio de Economía y Competitividad (MINECO) of Spain under Project MAT2013-47192-C3-1-R, and Generalitat Valenciana (PrometeoII/2014/020). O.A. acknowledges Generalitat Valenciana for a grant (GRISOLIAP2014/035). A.G. thanks MINECO for a Ramón y Cajal Fellowship (RYC-2014-16809). SCIC at UJI are also acknowledged.

■ REFERENCES

(1) Snath, H. J.; Abate, A.; Ball, J. M.; Eperon, G. E.; Leijtens, T.; Noel, N. K.; Stranks, S. D.; Wang, J. T.-W.; Wojciechowski, K.; Zhang,

W. Anomalous Hysteresis in Perovskite Solar Cells. *J. Phys. Chem. Lett.* **2014**, *5*, 1511–1515.

(2) Herman, M.; Jankovec, M.; Topič, M. Optimal I-V Curve Scan Time of Solar Cells and Modules in Light of Irradiance Level. *Int. J. Photoenergy* **2012**, *2012*, 151452.

(3) Albin, D. S.; del Cueto, J. A. In Effect of Hysteresis on Measurements of Thin-Film Cell Performance. In *Reliability of Photovoltaic Cells, Modules, Components, and Systems III*; Dhere, N. G., Wohlgemuth, J. H., Lynn, K., Eds; Proc. of SPIE, 2010; Vol. 7773.

(4) Azpiroz, J. M.; Mosconi, E.; Bisquert, J.; De Angelis, F. Defect migration in methylammonium lead iodide and its role in perovskite solar cell operation. *Energy Environ. Sci.* **2015**, *8*, 2118–2127.

(5) Dualeh, A.; Moehl, T.; Tétreault, N.; Teuscher, J.; Gao, P.; Nazeeruddin, M. K.; Grätzel, M. Impedance Spectroscopic Analysis of Lead Iodide Perovskite-Sensitized Solid-State Solar Cells. *ACS Nano* **2014**, *8*, 362–373.

(6) Sanchez, R. S.; Gonzalez-Pedro, V.; Lee, J.-W.; Park, N.-G.; Kang, Y. S.; Mora-Sero, I.; Bisquert, J. Slow Dynamic Processes in Lead Halide Perovskite Solar Cells. Characteristic Times and Hysteresis. *J. Phys. Chem. Lett.* **2014**, *5*, 2357–2363.

(7) Almora, O.; Zarazua, I.; Mas-Marza, E.; Mora-Sero, I.; Bisquert, J.; Garcia-Belmonte, G. Capacitive Dark Currents, Hysteresis, and Electrode Polarization in Lead Halide Perovskite Solar Cells. *J. Phys. Chem. Lett.* **2015**, *6*, 1645–1652.

(8) Tress, W.; Marinova, N.; Moehl, T.; Zakeeruddin, S. M.; Nazeeruddin, M. K.; Grätzel, M. Understanding the rate-dependent *J*-*V* hysteresis, slow time component, and aging in $\text{CH}_3\text{NH}_3\text{PbI}_3$ perovskite solar cells: the role of a compensated electric field. *Energy Environ. Sci.* **2015**, *8*, 995–1004.

(9) Unger, E. L.; Hoke, E. T.; Bailie, C. D.; Nguyen, W. H.; Bowring, A. R.; Heumüller, T.; Christoforo, M. G.; McGehee, M. D. Hysteresis and transient behavior in current-voltage measurements of hybrid-perovskite absorber solar cells. *Energy Environ. Sci.* **2014**, *7*, 3690–3698.

(10) Kim, H.-S.; Park, N.-G. Parameters Affecting I–V Hysteresis of $\text{CH}_3\text{NH}_3\text{PbI}_3$ Perovskite Solar Cells: Effects of Perovskite Crystal Size and Mesoporous TiO_2 Layer. *J. Phys. Chem. Lett.* **2014**, *5*, 2927–2934.

(11) Christians, J. A.; Manser, J. S.; Kamat, P. V. Best Practices in Perovskite Solar Cell Efficiency Measurements. Avoiding the Error of Making Bad Cells Look Good. *J. Phys. Chem. Lett.* **2015**, *6*, 852–857.

(12) Chen, B.; Yang, M.; Zheng, X.; Wu, C.; Li, W.; Yan, Y.; Bisquert, J.; Garcia-Belmonte, G.; Zhu, K.; Priya, S. Impact of Capacitive Effect and Ion Migration on the Hysteretic Behavior of Perovskite Solar Cells. *J. Phys. Chem. Lett.* **2015**, *6*, 4693–4700.

(13) Wei, J.; Zhao, Y.; Li, H.; Li, G.; Pan, J.; Xu, D.; Zhao, Q.; Yu, D. Hysteresis Analysis Based on the Ferroelectric Effect in Hybrid Perovskite Solar Cells. *J. Phys. Chem. Lett.* **2014**, *5*, 3937–3945.

(14) Forgacs, D.; Sessolo, M.; Bolink, H. J. Lead acetate precursor based p-i-n perovskite solar cells with enhanced reproducibility and low hysteresis. *J. Mater. Chem. A* **2015**, *3*, 14121–14125.

(15) Sepalage, G. A.; Meyer, S.; Pascoe, A.; Scully, A. D.; Huang, F.; Bach, U.; Cheng, Y.-B.; Spiccia, L. Copper(I) Iodide as Hole-Conductor in Planar Perovskite Solar Cells: Probing the Origin of *J*-*V* Hysteresis. *Adv. Funct. Mater.* **2015**, *25*, 5650–5661.

(16) Ip, A. H.; Quan, L. N.; Adachi, M. M.; McDowell, J. J.; Xu, J.; Kim, D. H.; Sargent, E. H. A two-step route to planar perovskite cells exhibiting reduced hysteresis. *Appl. Phys. Lett.* **2016**, *6*, 1502246.

(17) Almora, O.; Guerrero, A.; Garcia-Belmonte, G. Ionic charging by local imbalance at interfaces in hybrid lead halide perovskites. *Appl. Phys. Lett.* **2016**, *108*, 043903.

(18) Zarazua, I.; Bisquert, J.; Garcia-Belmonte, G. Light-Induced Space-Charge Accumulation Zone as Photovoltaic Mechanism in Perovskite Solar Cells. *J. Phys. Chem. Lett.* **2016**, *7*, 525–528.

(19) Carrillo, J.; Guerrero, A.; Rahimnejad, S.; Almora, O.; Zarazua, I.; Mas-Marza, E.; Bisquert, J.; Garcia-Belmonte, G. Ionic Reactivity at Contacts and Aging of Methylammonium Lead Triiodide Perovskite Solar Cells. *Adv. Energy Mater.* **2016**, DOI: [10.1002/aenm.201502246](https://doi.org/10.1002/aenm.201502246).

(20) Juarez-Perez, E. J.; Sanchez, R. S.; Badia, L.; Garcia-Belmonte, G.; Kang, Y. S.; Mora-Sero, I.; Bisquert, J. Photoinduced Giant

Dielectric Constant in Lead Halide Perovskite Solar Cells. *J. Phys. Chem. Lett.* **2014**, *5*, 2390–2394.

(21) Han, Y.; Meyer, S.; Dkhissi, Y.; Weber, K.; Pringle, J. M.; Bach, U.; Spiccia, L.; Cheng, Y.-B. Degradation observations of encapsulated planar $\text{CH}_3\text{NH}_3\text{PbI}_3$ perovskite solar cells at high temperatures and humidity. *J. Mater. Chem. A* **2015**, *3*, 8139–8147.

(22) Li, B.; Li, Y.; Zheng, C.; Gao, D.; Huang, W. Advancements in stability of perovskite solar cells: degradation mechanisms and improvement approaches. *RSC Adv.* **2016**, *6*, 38079–38091.

(23) Zhao, C.; Chen, B.; Qiao, X.; Luan, L.; Lu, K.; Hu, B. Perovskite Solar Cells: Revealing Underlying Processes Involved in Light Soaking Effects and Hysteresis Phenomena in Perovskite Solar Cells. *Adv. Energy Mater.* **2015**, *5*, 1500279.

(24) Jena, A. K.; Chen, H.-W.; Kogo, A.; Sanehira, Y.; Ikegami, M.; Miyasaka, T. The Interface between FTO and the TiO_2 Compact Layer Can Be One of the Origins to Hysteresis in Planar Heterojunction Perovskite Solar Cells. *ACS Appl. Mater. Interfaces* **2015**, *7*, 9817–9823.

(25) Bisquert, J. *Nanostructured Energy Devices: Equilibrium Concepts and Kinetics*; CRC Press Taylor & Francis Group: Boca Raton, FL, 2014.

(26) Jung, H. S.; Park, N.-G. Perovskite Solar Cells: From Materials to Devices. *Small* **2015**, *11*, 10–25.

(27) Kim, H.-S.; Jang, I.-H.; Ahn, N.; Choi, M.; Guerrero, A.; Bisquert, J.; Park, N.-G. Control of I–V Hysteresis in $\text{CH}_3\text{NH}_3\text{PbI}_3$ Perovskite Solar Cell. *J. Phys. Chem. Lett.* **2015**, *6*, 4633–4639.

(28) Stoumpos, C. C.; Malliakas, C. D.; Kanatzidis, M. G. Semiconducting Tin and Lead Iodide Perovskites with Organic Cations: Phase Transitions, High Mobilities, and Near-Infrared Photoluminescent Properties. *Inorg. Chem.* **2013**, *52*, 9019–9038.

(29) Roiati, V.; Mosconi, E.; Listorti, A.; Colella, S.; Gigli, G.; De Angelis, F. Stark Effect in Perovskite/ TiO_2 Solar Cells: Evidence of Local Interfacial Order. *Nano Lett.* **2014**, *14*, 2168–2174.

(30) Rajagopal, A.; Williams, S. T.; Chueh, C.-C.; Jen, A. K. Y. Abnormal Current–Voltage Hysteresis Induced by Reverse Bias in Organic–Inorganic Hybrid Perovskite Photovoltaics. *J. Phys. Chem. Lett.* **2016**, *7*, 995–1003.

(31) Xu, J.; Buin, A.; Ip, A. H.; Li, W.; Voznyy, O.; Comin, R.; Yuan, M.; Jeon, S.; Ning, Z.; McDowell, J. J.; Kanjanaboos, P.; Sun, J.-P.; Lan, X.; Quan, L. N.; Kim, D. H.; Hill, I. G.; Maksymovych, P.; Sargent, E. H. Perovskite–fullerene hybrid materials suppress hysteresis in planar diodes. *Nat. Commun.* **2015**, *6*, 7081.

(32) Torres, C. I.; Marcus, A. K.; Parameswaran, P.; Rittmann, B. E. Kinetic Experiments for Evaluating the Nernst–Monod Model for Anode-Respiring Bacteria (ARB) in a Biofilm Anode. *Environ. Sci. Technol.* **2008**, *42*, 6593–6597.

(33) Bryant, D.; Wheeler, S.; O'Regan, B. C.; Watson, T.; Barnes, P. R. F.; Worsley, D.; Durrant, J. Observable Hysteresis at Low Temperature in “Hysteresis Free” Organic–Inorganic Lead Halide Perovskite Solar Cells. *J. Phys. Chem. Lett.* **2015**, *6*, 3190–3194.

(34) Yu, H.; Lu, H.; Xie, F.; Zhou, S.; Zhao, N. Native Defect-Induced Hysteresis Behavior in Organolead Iodide Perovskite Solar Cells. *Adv. Funct. Mater.* **2016**, *26*, 1411–1419.

(35) Zou, Y.; Holmes, R. J. Temperature-Dependent Bias Poling and Hysteresis in Planar Organo-Metal Halide Perovskite Photovoltaic Cells. *Adv. Energy Mater.* **2016**, *6*, 1501994.

(36) Ono, L. K.; Raga, S. R.; Wang, S.; Kato, Y.; Qi, Y. Temperature-dependent hysteresis effects in perovskite-based solar cells. *J. Mater. Chem. A* **2015**, *3*, 9074–9080.

(37) Guerrero, A.; You, J.; Aranda, C.; Kang, Y. S.; Garcia-Belmonte, G.; Zhou, H.; Bisquert, J.; Yang, Y. Interfacial Degradation of Planar Lead Halide Perovskite Solar Cells. *ACS Nano* **2016**, *10*, 218–224.

(38) Weber, D. $\text{CH}_3\text{NH}_3\text{PbX}_3$, a Pb(II)-System with Cubic Perovskite Structure. *Z. Naturforsch., B: J. Chem. Sci.* **1978**, *33b*, 1443–1445.

(39) Ahn, N.; Son, D.-Y.; Jang, I.-H.; Kang, S. M.; Choi, M.; Park, N.-G. Highly Reproducible Perovskite Solar Cells with Average Efficiency of 18.3% and Best Efficiency of 19.7% Fabricated via Lewis Base Adduct of Lead(II) Iodide. *J. Am. Chem. Soc.* **2015**, *137*, 8696–8699.